

pubs.acs.org/JPCC Article

Dynamic Quantum-State Renormalization and Effects of Competing Pathways on Carrier Relaxation in Semiconductor Nanoparticles

Jie Chen, William M. Sanderson, and Richard A. Loomis*



Cite This: J. Phys. Chem. C 2023, 127, 20082–20093



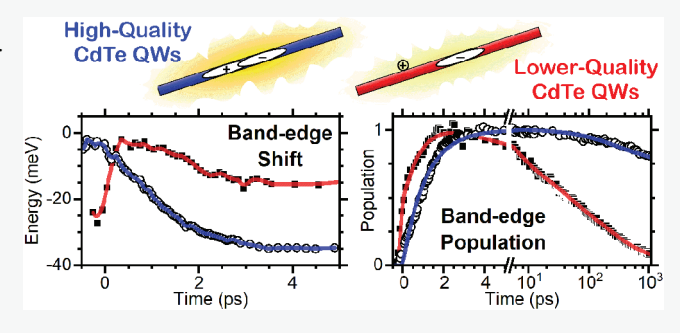
ACCESS

III Metrics & More

Article Recommendations

Supporting Information

ABSTRACT: The magnitude and temporal evolution of the quantum-state renormalization (QSR), or the energetic shifting of the quantum-confinement states caused by photoexcitation and changes in electron screening, were probed in transient absorption (TA) spectroscopy measurements of colloidal semiconductor nanoparticles. Experiments were performed on high- and lower-quality wurtzite CdTe quantum wires (QWs) with photoluminescence quantum yields of 8.8% and ~0.2% using low-excitation fluences. The QSR shifts the spectral features to lower energies in both samples, with larger shifts measured in the high-quality QWs. The TA spectral features measured for both samples



shift uniquely with time after photoexcitation, illustrating dynamic QSR that depends on the quantum-confinement states and on the states occupied by carriers. The higher fraction of carriers that reach the band-edge states in the high-quality QWs results in larger renormalization, with the energies of the band-edge states approaching the Stokes shift of the steady-state photoluminescence feature below the band-edge absorption energy. The intraband relaxation dynamics of charge carriers photoexcited in semiconductor nanoparticles was also characterized after accounting for contributions from QSR in the TA data. The intraband relaxation to the band-edge states was slower in the high-quality QWs than in the lower-quality QWs, likely due to the reduced number of trap states accessible. The contrasting relaxation time scales provide definitive evidence for a dependence of the photoluminescence efficiency on excitation energy. These studies reveal the complicated interplay between the energetics and relaxation mechanisms of carriers within semiconductor nanoparticles, even those with the same dimensionality.

■ INTRODUCTION

The ability to tune band gap energies by varying the size and thus the quantum confinement of charge carriers within semiconductor nanoparticles (NPs) coupled with the synthetic capabilities to achieve extremely high photoluminescence quantum yields (Φ_{PL}) have led to their implementation in solar cells, lasers, photodetectors, and bioimaging. 1-5 It would be ideal for every photon that impinges on a device to be absorbed by the NPs, and each photogenerated electron-hole pair to relax to the band-edge states, regardless of the energy of the photon absorbed. Once the carriers reach these states, either they would, depending on the application, radiatively recombine with a Φ_{PL} of unity or the electron and hole would be separately collected as current with little or no loss of energy within the system. The densities of the states within the NPs, the energies of these states, and the intraband relaxation mechanisms all play factors into how ideal these NPs can perform. Additional complications can arise as the delocalized nature of the charge carriers in NPs and their large surface-tovolume ratios make their optical and electronic properties highly dependent on the dimensionality, surface ligation, and local environment of the NPs. 6-11

Despite broad interdisciplinary interests in semiconductor NPs, open questions remain over the energetics and dynamics

of photoexcited charge carriers as they relax to the band-edge states in these nanomaterials. For instance, the energies of the band-edge states and even higher-energy quantum-confinement states shift after photoexcitation, but a clear understanding of the origins of this shifting is not broadly accepted. Phenomena including Stark effects, ^{12–16} the stabilization of biexcitons, ^{14–25} and band gap renormalization (BGR)^{26–31} have been associated with the shifting of the band-edge states after photoexcitation, especially when multiple electron—hole pairs are photoexcited in the NPs. We recently introduced the concept of quantum-state renormalization (QSR) associated with the energetic shifting of the quantum-confinement states in colloidal semiconductor NPs that occurs with photoexcitation and is observed in transient absorption (TA) spectroscopy experiments. ^{32,33}

Received: August 22, 2023 Revised: September 17, 2023 Published: October 2, 2023





In many regards, QSR is akin to the renormalization of the band-edge states characterized in the monolayer transition metal dichalcogenides (TMDCs). 34-41 Time- and angleresolved photoemission spectroscopy experiments performed on room-temperature monolayer MoS2 directly probed the electronic structure renormalization induced with low excitation fluences. 34,35 The band-edge states of the MoS₂ sample were observed to shift by ~40 meV to higher energies at the K point, $k = -1.29(1) \text{ Å}^{-1}$, upon photoexcitation with low fluences, followed by a recovery within 5.0(1.8) ps. The excitation energy at the K valley edge, $k = -1.14(1) \text{ Å}^{-1}$, was observed to decrease by ~100 meV, and this perturbation remained for much longer than that at the K point. Supporting calculations indicate the photoexcitation and formation of excitons alters carrier screening in the semiconductor, and increases in the effective masses of the conduction band (CB) and valence band (VB) states, and a renormalization of their energies result. 34,35 The larger effective masses of the carriers result in a flattening of the MoS2 monolayer bands and the observed increase in the band gap energy at the K point and the energetic decrease at the K valley edge.

A quick overview of quantum confinement in semiconductor NPs is provided to illustrate the ramifications of QSR. The edges of the VB and CB, which tend to dictate the optical response of semiconductors, are commonly modeled by using the effective mass approximation (EMA). The EMA assumes the bands are parabolic with k, the wave vector along the orthogonal directions within the crystalline semiconductor, according to $E(k) = \hbar^2 k^2 / (2 m_e m^*)$, where the effective mass, m^* , is a scaling parameter for the mass of the electron, m_e . 42,43 When the size of the semiconductor is reduced to scales on the order of the de Broglie wavelength of the carriers, the motion and energies of the carriers along that direction become quantized. This quantization selects unique values of k and energy along E(k) that are allowed.⁴² This is depicted by the black points on the parabolic band plotted in Figure 1a. The confinement dimension for the schematic shown is along z, and n_z identifies the different quantum-confinement states. The confinement energies and states are often approximated as the solutions for the quantum-mechanical particle-in-a-box problem for both the VB and CB, as shown in Figure 1c. The energies along the other unconfined coordinates follow the EMA with parabolic bands associated with each quantum confinement state, depicted as blue bands in Figure 1a and b. The total energy of a carrier in this system is the sum of the quantum-confinement energy along z and the translational energy along x and y.

The absorption of a photon with sufficient energy promotes an electron from a quantum state in the VB to one in the CB, and a hole or electron deficiency is simultaneously formed in the VB state. This photoexcitation results in changes in electron screening, shielding, and electron-electron interactions in comparison to the unexcited semiconductor that alter the energetics of the VB and CB, and thus the effective masses of the carriers, in the spatial region of the NP sampled by the electron-hole pair, as depicted by the red bands in Figure 1d. As mentioned above, this photoinduced increase in the effective masses of the carriers is observed and well modeled in monolayer TMDCs, although the band structure for those systems leads to an increase in the band gap energy. 34,35 Since the energies of the quantum-confinement states depend on the effective masses of the carriers, the quantum-confinement states in the VB and CB energetically shift with photo-

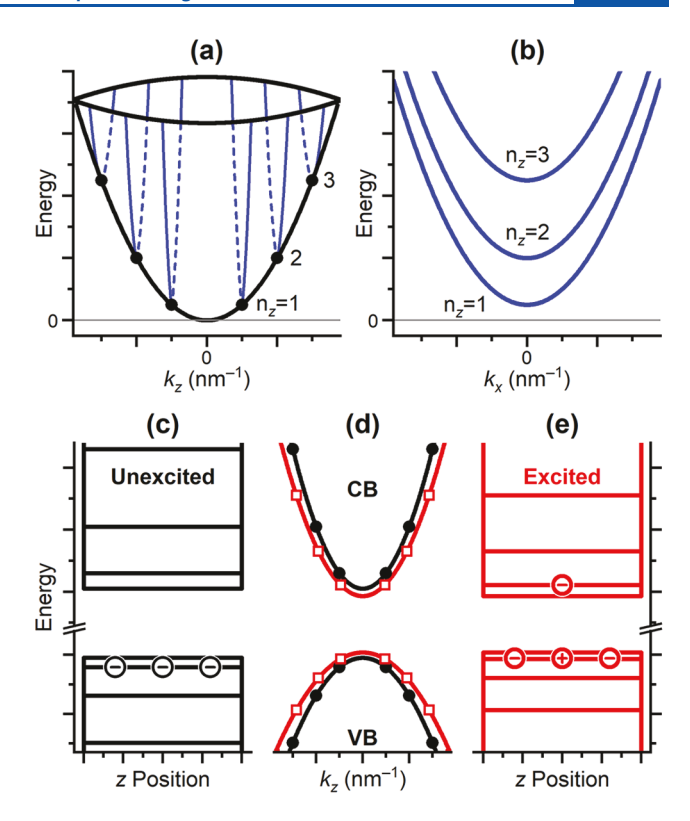


Figure 1. Schematic of quantum-state renormalization for a semiconductor NP with confinement along the z direction. (a) Representation of a parabolic band along k_z for the conduction band (CB) following the effective mass approximation.⁴³ Confinement along z leads to discrete values of $E(k_z)$ dictated by the lattice parameter and effective mass. (b) The confinement along z leads to discrete bands k_x and k_y (not shown) for each n_z . (c) This confinement can be approximated as a quantum-mechanical particle-in-a-box (PIB) for both the CB and the valence band (VB). Photoexcitation of an electron from the VB to the CB alters electron screening and shielding and changes in the effective masses for the VB and CB result, (d). As a result, the bottom of the potential and the PIB states shift with photoexcitation (e), and these are probed in transient absorption spectroscopy measurements. The radiative recombination of electron-hole pairs occurs from the lowest-energy shifted states.

excitation, even with the presence of only a single electronhole pair in each NP, as depicted in Figure 1e. Photoexcited electrons, holes, and excitons may also interact with the ions in a polar semiconductor nanocrystal through Fröhlich interactions. 44-56 The photoexcited electron and hole interact with the cations and anions in the crystal lattice, perturbing the crystal structure and coupling with longitudinal optical (LO) phonons. 53-59 The changes in the crystal structure that result from these Fröhlich interactions result in contrasting electronic band structures and effective masses for the CB and VB in the unexcited and excited semiconductor NPs. 44-48,56,60-62 These energetic shifts are grouped together as QSR. Since the different quantum-confinement states have unique spatial probability densities, each state, including those that are occupied or not, should experience unique QSR that depend on the states in the VB and CB that are occupied. 54,55 As a result, the QSR of the quantum-confinement states should be dynamic, as the carriers relax through the energetically accessible states after photoexcitation. Finally, the QSR should

also depend on carrier density and if the electrons and holes are bound as excitons or are separate free carriers.

A TA spectroscopy experiment performed on a sample of semiconductor NPs will yield temporal and spectral data that contain bleach signals associated with the quantum-confinement states of the unexcited NP, black in Figure 1c, induced-absorption signals associated with the shifted states, red in Figure 1e, and bleach signals associated with the occupation of either electrons or holes in the different quantum-confinement states. When electrons and holes are photoexcited above the band-edge states, the carriers undergo intraband relaxation through the energetically accessible quantum-confinement states, and the QSR for all of the states should be dynamic.

Herein, we report on the contrasting dynamic nature of QSR measured using time-resolved TA spectroscopy on two samples of NPs, specifically wurtzite (WZ) cadmium telluride (CdTe) quantum wires (QWs), with nearly the same dimensionality but notably different values of $\Phi_{\rm PL}$. The CdTe QWs were chosen for these studies for several reasons. First, the fine structure of the hole states in one-dimensional QWs results in the lowest-energy transitions being optically bright, instead of dark, which is common for quantum dots. 63-66 Thus, the carrier populations relax to and emit from these lowest-energy states, and bleach and stimulated emission signals present in the TA data are indistinguishable, with both negating the induced-absorption signals of the shifted band-edge states. While the absorption cross sections of QWs are larger than those of quantum dots, because of their larger volumes, the increase in volume and the free degree of freedom also reduce the interactions of carriers photogenerated by different photons. Lastly, our previous efforts on QSR in CdTe QWs revealed that the contributions of QSR in TA data can be largely accounted for using a simple model that incorporates the steady-state absorption spectrum of the QWs. 32,33

Specifically, time-resolved TA spectroscopy experiments were performed on high-quality and lower-quality WZ CdTe QWs with average diameters and photoluminescence (PL) efficiencies of \sim 6 nm and $\Phi_{\rm PL}$ = 8.8% and \sim 7.5 nm and $\Phi_{\rm PL}$ = 0.2%, respectively. The temporal dependencies of the energies of the spectral features and the occupation of carriers in the states associated with those features were identified in the TA data, $\Delta {\rm Abs_{TA}}(E,\,t)$, as previously described. The magnitude of the QSR observed in the two QW samples is distinctly different, and contrasting QSR energies and temporal dependencies were identified for the spectral features of each sample.

METHODS

Chemicals. Tri-*n*-octylphosphine (TOP, 90%, Aldrich), tri-*n*-octylphosphine oxide (TOPO, 99%, Aldrich), 1-octadecene (ODE, 90%, Aldrich), ethanethiol (EtSH, 97%, Aldrich), tellurium granules (Te, -5-+50 mesh, 99.99%, Aldrich), and cadmium acetate dihydrate (Cd(acetate)₂·2H₂O, 99.9%, Mallinckrodt) were used as received. Cd(di-*n*-octylphosphinate)₂, tri-*n*-octylphosphine telluride (TOP-Te) stock solution (0.025 mmol g⁻¹ solution), di-*n*-octylphosphinate (DOP) stock solution, and bismuth (Bi) NP stock solutions (0.04 mmol Bi atoms g⁻¹ solution) were prepared following literature methods.

CdTe QW Sample Preparation. Colloidal CdTe QWs with WZ crystal structures were synthesized using the solution—solid—solid (SSS) method previously reported.⁶⁷ The CdTe QW syntheses were performed under nitrogen

 (N_2) gas protection. The as-synthesized, lower-quantum yield CdTe QWs were grown using 9.1-nm-diameter bismuth NPs at 250 °C in the presence of di-n-octylphosphine (0.14 mol %). Cd(di-n-octylphosphinate)₂ and tri-n-octylphosphine telluride (TOPTe, 0.025 mmol g^{-1}) were used as the Cd and Te precursors with a Cd:Te precursor mole ratio of 2.8. The average diameter of these QWs was determined to be \sim 7.5 nm by measuring the widths of individual QWs in transmission electron microscopy images. The ensemble PL efficiency of these QWs was measured to be $\Phi_{\rm PL}=0.2\%$ with excitation at 2.76 eV. After synthesis, the CdTe QWs were stored in a nitrogen-purged glovebox until the steady-state and time-resolved spectroscopy experiments were performed. Figure S1 in the Supporting Information includes a typical TEM image of the as-synthesized CdTe QWs.

The sample of high-quantum yield, $\Phi_{PL} = 8.8\%$, CdTe QWs with a mean diameter of 6 nm, and predominant WZ crystal structure was also prepared. For this sample, 31 mg of Cd(di-noctylphosphinate)₂ and 4.0 g of purified trin-octylphosphine oxide (TOPO) were loaded into a 50 mL Schlenk reaction tube, degassed for 1 h, and then heated to 300 °C. 22 mg of the 6.3 nm Bi NP stock solution, 898 mg of TOP-Te stock solution, and 101 mg of DOP stock solution were combined and quickly injected into a Schlenk tube. The reaction was stopped after 2 min, and the sample was cooled to room temperature. A PL-enhancement treatment 11 was then performed on these as-synthesized CdTe QWs. The obtained PL-enhanced CdTe QWs were suspended in TOP for further characterization and measurements.

Steady-State Spectroscopy. The steady-state extinction spectra were collected by using a commercial UV-vis-NIR spectrometer with an integration sphere to minimize contributions from scattering. A scattering background was still observed in the spectra of most of the QWs, and this contribution was subtracted from the extinction spectra (Figure S2 in Supporting Information) using previously reported methods. 32,33 The photoluminescence (PL(E)) spectra and Φ_{PL} values were measured by using a commercial spectrofluorometer system (Horiba-Nanolog). The PL spectra were recorded using excitation at 2.76 eV (450 nm). The absorption value of the CdTe QWs was kept under a 0.1 OD at 2.76 eV during the Φ_{PL} measurements to reduce selfabsorption and PL quenching. The peaks of the features present in the absorption spectra that are associated with groups of quantum-confinement transitions were identified using the second derivative of the absorption spectrum, as illustrated in Figure S3 in Supporting Information.

The PL efficiency spectra were collected and cross-verified using two different methods described previously. 69,70 The first method is a direct measurement where the $\Phi_{\rm PL}$ values were measured at discrete excitation energies, E, using a commercial spectrofluorimeter system (Horiba-Nanolog) to obtain the $\Phi_{\rm PL}(E)$ spectrum. The second method is a relative method and involves calculating the PL efficiency spectrum ${\rm PL}_{\rm Eff}(E)$. Here, the steady-state spectrum, ${\rm Abs}_{\rm SS}(E)$, and the PL excitation spectrum, ${\rm PLE}(E)$, were collected by using commercial spectrometers. The ${\rm PL}_{\rm Eff}(E)$, is the ratio of the ${\rm PLE}(E)$ spectrum to the absorptance spectrum, or

$$PL_{Eff}(E) = \frac{PLE(E)}{1 - 10^{-Abs_{SS}(E)}}$$

The relative scale of each $PL_{Eff}(E)$ spectrum can be quantified to an absolute scale by normalizing the spectrum to measurements of Φ_{PL} values at discrete excitation energies throughout the spectral region for each sample.

Transient Absorption Spectroscopy. Femtosecond time-resolved TA measurements were conducted using an amplified titanium:sapphire femtosecond laser and a commercial TA spectrometer. The 800 nm fundamental pulses (0.100 ps, 1.55 eV (800 nm), 1 kHz repetition rate) generated from the amplifier laser were split into two parts. A minor fraction, 5%, of the 1.55 eV beam was focused into a sapphire crystal, generating a white-light continuum spanning 1.63-2.76 eV (450-760 nm) as probe light. The rest of the fundamental output was used to pump an optical parameter amplifier (OPA) to generate excitation pulses at 2.76 eV. The excitation pulses were then depolarized. A motorized delay stage was used to control the delay time (up to 7 ns) between the excitation and the white-light probe pulses. The instrumentresponse function was well fit to a Gaussian with a full-width half-maximum breadth of 0.230 ps, with a slight dependence on photon energy within the white-light spectrum. The TA spectrum at each time delay was averaged over 2 s, and variable step sizes were used with smaller step sizes used near t = 0 s. The TA spectra were corrected for background noise, scattering light, and spectral chirp. All of the TA measurements were performed in air at room temperature.

Excitation Laser Fluence Dependence. The TA measurements for the high-quality WZ CdTe QWs were conducted by using excitation fluences from 4 to 15 μ J cm⁻² pulse⁻¹. The temporal profiles of the $1\Sigma'$ feature at 1.75 eV in the TA data collected using low and high pump fluence are compared in Figure S5 in Supporting Information to identify contributions of multicarriers in the QWs. The temporal profiles collected with a fluence below 6 μ J cm⁻² pulse⁻¹ exhibit minimal differences in the profiles. Therefore, multicarrier interactions in the CdTe QWs are negligible with an excitation fluence of 4 μ J cm⁻² pulse⁻¹. The average number of electron-hole pairs photoexcited within a single QW were calculated in the same manner reported previously,³³ and details are provided in Supporting Information. A fluence of 4 μ J cm⁻² pulse⁻¹ resulted in the photogeneration of ~10 excitons μm^{-1} pulse⁻¹ in each QW for the Φ_{PL} = 8.8% QWs. An excitation fluence of $\sim 10 \ \mu J \ cm^{-2} \ pulse^{-1}$ was used for the TA measurements on the Φ_{PL} = 0.2% QWs, as described previously.³³ A significantly higher carrier density of ~75 excitons μm^{-1} pulse⁻¹ were prepared in each QW in the largerdiameter, Φ_{PL} = 0.2% QWs.

RESULTS

Steady-State Spectroscopy. Steady-state absorption spectra, $Abs_{SS}(E)$, of the CdTe QWs, Figure 2, were collected to identify excitation features and for use in modeling the QSR.³² Each absorption feature is associated with groups of transitions with assignments guided by theory.^{32,33} Due to significant state mixing in the VB, the absorption features are labeled with the quantum-confinement state(s) accessed in the CB, specifically the 1Σ , 1Π , $1\Delta/2\Sigma$, and $1\Phi/2\Pi/1\Gamma$ states.^{32,33} Most of the band-edge transitions lie within the 1Σ feature, but calculations indicate that there is also one transition between the lowest-energy 1Σ hole state and the 1Π electron state on the lower-energy side of the 1Π feature. The very weak $1\Sigma^*$ feature, near 1.8 eV in both spectra, is associated with a transition between an excited hole state and the 1Σ electron

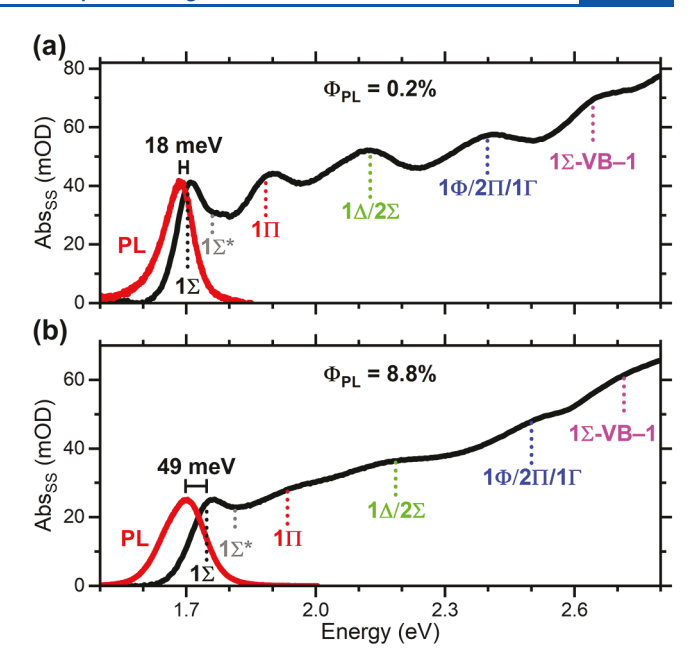


Figure 2. Steady-state absorption (black) and PL (red) spectra of (a) lower-quality $\Phi_{PL}=0.2\%$ and (b) high-quality $\Phi_{PL}=8.8\%$ WZ CdTe QWs. The tics mark the centers of the steady-state absorption features, and the labels are the quantum-confinement states accessed in the conduction band by the transitions within each feature. 32,33

state. The 1Π , $1\Delta/2\Sigma$, and $1\Phi/2\Pi/1\Gamma$ features each contain numerous transitions between excited electron and hole quantum-confinement states. The 1Σ -VB-1 feature centered above 2.7 eV contains transitions between the 1Σ electron state in the CB and the hole states within the VB-1 band, and it overlaps other high-energy transitions within the VB.

The PL(E) spectra of the CdTe QWs are also plotted in Figure 2a, b. The high-quality $\Phi_{\rm PL}=8.8\%$ WZ CdTe QWs have a larger PL Stokes shift than the lower-quality $\Phi_{\rm PL}=0.2\%$ QWs, 49 versus 18 meV. PL efficiency spectra of the QWs, Figure S4 in Supporting Information, were recorded in a manner described previously. There is a monotonic decrease in efficiency with increasing excitation energy for the high-quality QWs that indicates the number of non-radiative traps increases with energy above the band gap energy. The PL_{Eff}(E) spectrum for the lower-quality QWs is notably different from local minima and maxima. This trend indicates there are nonradiative traps at localized energies that are accessed during photoexcitation, but not while the carriers relax through these energies to the band-edge states. To

Transient Absorption Spectroscopy. The TA data, $\Delta {\rm Abs_{TA}}(E,\ t)$, plotted in Figure 3a, b, contain overlapping induced-absorption (positive, red) and bleach (negative, yellow to blue) signals. Stimulated emission signals are also likely present in these data, and these are not separable from the bleach signals associated with excited-state populations. The most prominent signals in these data are the long-lived bleach signals near the energies of the $1\Sigma \ {\rm Abs_{SS}}(E)$ feature, black arrow just above 1.7 eV. There are much weaker and shorter-lived, <3 ps, bleach signals near the other ${\rm Abs_{SS}}(E)$ features, indicated by the red, green, and blue arrows. The energies of these bleach signals shift slightly with time due to the energetic shifting of the signals (frequency modulation) or the contrasting time scales of overlapping signals (amplitude modulation).

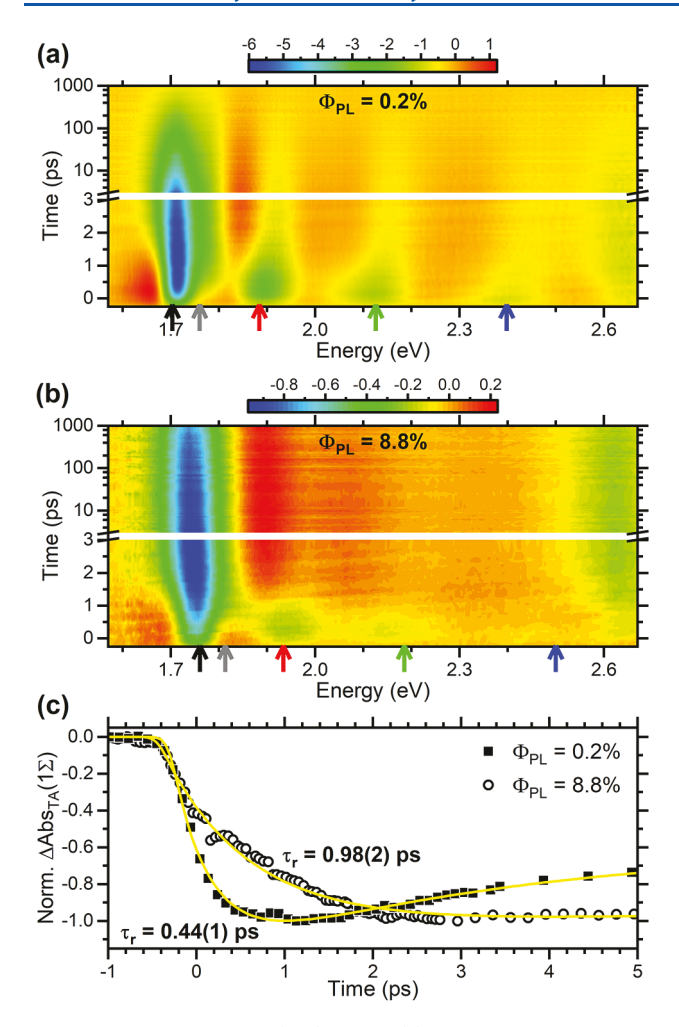


Figure 3. TA data, $\Delta {\rm Abs_{TA}}(E,\,t)$, of the (a) lower-quality $\Phi_{\rm PL}=0.2\%$ and (b) high-quality $\Phi_{\rm PL}=8.8\%$ WZ CdTe QWs. The excitation energy was 2.76 eV. The color scales are mOD, and there are breaks in the time axes at 3 ps, after which a log scale is used. The arrows are the energies of the ${\rm Abs_{SS}}(E)$ features. (c) Temporal profiles of the 1Σ bleach features for the two samples. Each 1Σ profile was fit (yellow) to a sum of a single-exponential rise, time constant $\tau_{\rm r}$, and multiexponential decays.

The temporal profiles of the 1Σ band-edge TA bleach signals are included in Figure 3c, and these were each fit to a sum of a single-exponential rise, with a time constant of τ_r , and three exponential decays. The rise time for the lower-quality Φ_{PL} = 0.2% QW sample is notably shorter than that for the highquality $\Phi_{\rm pL} = 8.8\%$ sample, $\tau_{\rm r} = 0.44(1)$ ps versus $\tau_{\rm r} = 0.98(2)$ ps. The rise times of these bleach signals are typically associated with the time scales for IRD to the band-edge states. These time constants suggest that the IRD from the higher-energy states to the 1Σ band-edge states is much faster in the lower-quality QWs due to the presence of the competing pathways associated with additional trap sites. The decay times are associated with interband relaxation and the lifetimes of the carriers in the QWs. The decay times of the 1Σ bleach signals for the high-quality CdTe QW sample are notably longer than those for the lower-quality CdTe QW sample, as expected with the higher Φ_{PL} value and a reduction of the density of nonradiative trap states. We emphasize that these data should not be taken quantitatively to represent the relaxation times of the carriers as contributions from QSR have not been accounted for.

Modeling Quantum-State Renormalization. A simple model for approximating the contributions of QSR and carrier occupation in $\Delta Abs_{TA}(E, t)$ data was recently reported.³² This model assumes that the $Abs_{ss}(E)$ spectrum becomes bleach signals in the $\Delta Abs_{TA}(E, t)$ data as the quantum-confinement states are energetically shifted following photoexcitation. The shifted states give rise to induced-absorption signals, $Abs_{IA}(E_t)$ t). The model initially assumes that the QSR shifts all of the transitions to lower energies by the same amount, $\Delta E_{\rm OSR}(t)$, and $Abs_{IA}(E, t) = Abs_{ss}(E - \Delta E_{QSR}(t))$. The average QSR shifts obtained for the Φ_{PL} = 0.2% and 8.8% CdTe QW samples are $\langle \Delta E_{OSR}(t) \rangle = 13(1)$ and 21.0(1.0) meV. The difference between $\Delta Abs_{OSR}(E, t)$ and $\Delta Abs_{TA}(E, t)$ at each t yields the bleach signals attributed to carrier populations within each of the QSR-shifted features. The occupancy spectrum at each time, which contains only those spectral features with an electron, hole, or exciton occupying a state in the CB or VB at that time, is proportional to the negative of this difference, $\Delta Abs_{Occ}(E, t) = \Delta Abs_{QSR}(E, t) - \Delta Abs_{TA}(E, t).$

The 2D color-contour plot containing the $\Delta {\rm Abs_{Occ}}(E,\ t)$ data for the high-quality $\Phi_{\rm PL}$ = 8.8% QWs is included in Figure 4a, and the $\Delta {\rm Abs_{Occ}}(E,\ t)$ spectra at multiple times are plotted

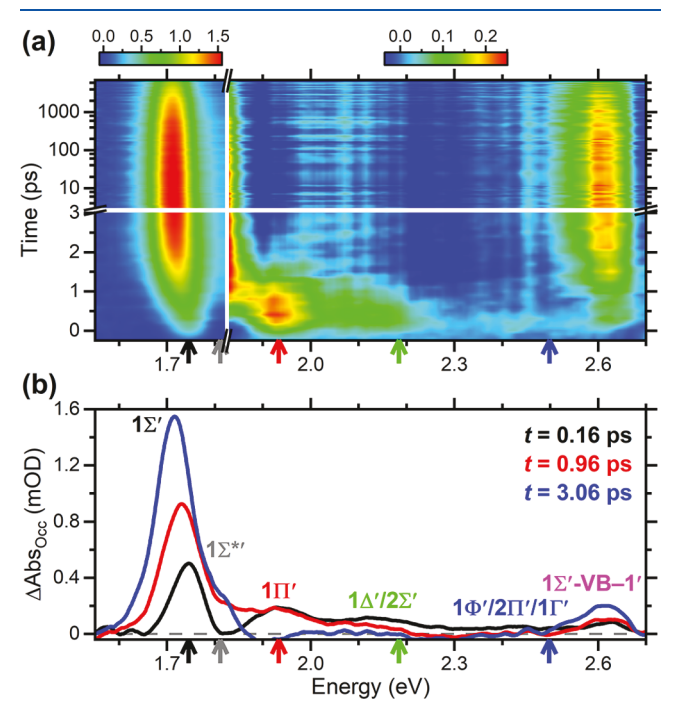


Figure 4. (a) 2D color-contour plot of the $\Delta \mathrm{Abs}_{\mathrm{Occ}}(E,\ t)$ data for high-quality $\Phi_{\mathrm{PL}}=8.8\%$ WZ CdTe QWs. The color scales are in units of mOD with a magnified scale above 1.82 eV. The time axis is log for t>3 ps. (b) $\Delta \mathrm{Abs}_{\mathrm{Occ}}(E,\ t)$ spectra at multiple times. The energies of the steady-state absorption features are indicated with arrows.

in Figure 4b. Each occupancy feature is labeled using the state(s) accessed in the CB as in the $Abs_{SS}(E)$ spectrum, but with a prime to signify the features are energetically shifted by QSR. At the shortest times, t < 1 ps, the spectra contain signals in all of the occupancy features, indicating there were carriers in the electron or hole quantum-confinement states associated with these features. The signals of the higher-energy features decay faster than the lower-energy features, and the lowest-energy $1\Sigma'$ band-edge feature grows in with time out to $t \approx 3$ ps, and then it slowly decays. These trends are consistent with

intraband relaxation and state filling. Similar data were obtained for the lower-quality Φ_{PL} = 0.2% WZ CdTe QWs.³³

The $\Delta {\rm Abs}_{{\rm Occ}}(E,\,t)$ spectrum at each t was fit to a sum of Gaussian peaks, one for each occupancy feature, as illustrated in Figure S9 in Supporting Information. The center energy of each Gaussian peak was recorded as a function of time to identify changes in the QSR, frequency modulation, or the contrasting contributions from the transitions within that feature that occur during carrier relaxation, amplitude modulation. The integrated area of each Gaussian is proportional to the weighted sum of the carrier occupancies in the quantum-confinement states associated with those transitions lying within each feature at that time. The IRD of the photoexcited carriers, either one electron, one hole, or one exciton, was tracked by plotting the carrier occupancies versus time after photoexcitation.

DISCUSSION

Dynamic QSR. The dissimilar spatial distributions of the different quantum-confinement states should result in contrasting screening and unique QSR for the occupied states as well as those for the unoccupied sates, both of which are probed in the TA experiments. 32,33 As mentioned, the average QSR values obtained from fitting the TA data a long times are $\langle \Delta E_{\rm QSR}(t) \rangle$ = 13(1) and 21.0(1.0) meV for the $\Phi_{\rm PL}$ = 0.2% and 8.8% CdTe QWs. The energies of the individual occupancy features indicate that the QSRs of the different quantum-confinement states are not the same, however, and the energies of the features do change uniquely with time after photoexcitation as the carriers relax to the band-edge states. The observation of unique $\Delta E_{OSR}(t)$ values for the different spectral features indicates a more thorough model for separating QSR from carrier populations in the TA data is needed to more accurately characterize the shifted state energies and carrier populations.

The $1\Sigma'$ occupancy feature for the lower-quality Φ_{PL} = 0.2% WZ CdTe QWs, solid squares in Figure 5a, is shifted to $\Delta E_{\rm Occ}(t) \approx 25$ meV below the energy of the 1 Σ steady-state absorption feature near t = 0 ps during the excitation pulse.³³ An estimate of \sim 75 electron/hole pairs μ m⁻¹ pulse⁻¹ were photoexcited within each QW, but the PL efficiency spectrum of the Φ_{PL} = 0.2% CdTe QWs, Figure S4a in Supporting Information, indicates that the relaxation of the carriers to the band edge state is not unity. With that said, most of the hole trapping occurs at the band-edge states. Comparison of the temporal profiles of the $1\Sigma'$, $1\Sigma^{*'}$, and the high-energy $1\Sigma'$ -VB-1' occupancy features indicates the signals at short times are associated with holes in the band-edge states that have not become trapped outside of the QWs.³³ Consequently, this prompt energy shift of the $1\Sigma'$ occupancy feature in the Φ_{PL} = 0.2% sample is associated with holes that quickly relaxed through the quantum-confinement states within the CB just above the band-edge state, as illustrated in the black energystate diagram in Figure 5c. If the low PL efficiency for these Φ_{PL} = 0.2% QWs is attributed only to trapping of holes in the band-edge states, then there are ~ 0.15 holes μm^{-1} pulse⁻¹ that radiatively recombine with electrons. The large density of hole traps present in the band-edge states results in short lifetimes for most of the holes, <3 ps, and $\Delta E_{\rm Occ}(t)$ of the $1\Sigma'$ feature decreases toward zero on that time scale. As electrons, both free electrons and those bound in excitons, relaxed to the $1\Sigma'$ quantum-confinement state in the CB, the $\Delta E_{\rm Occ}(t)$ of the $1\Sigma'$ feature slowly adjusted to a long-time value of 15.9(4) meV.

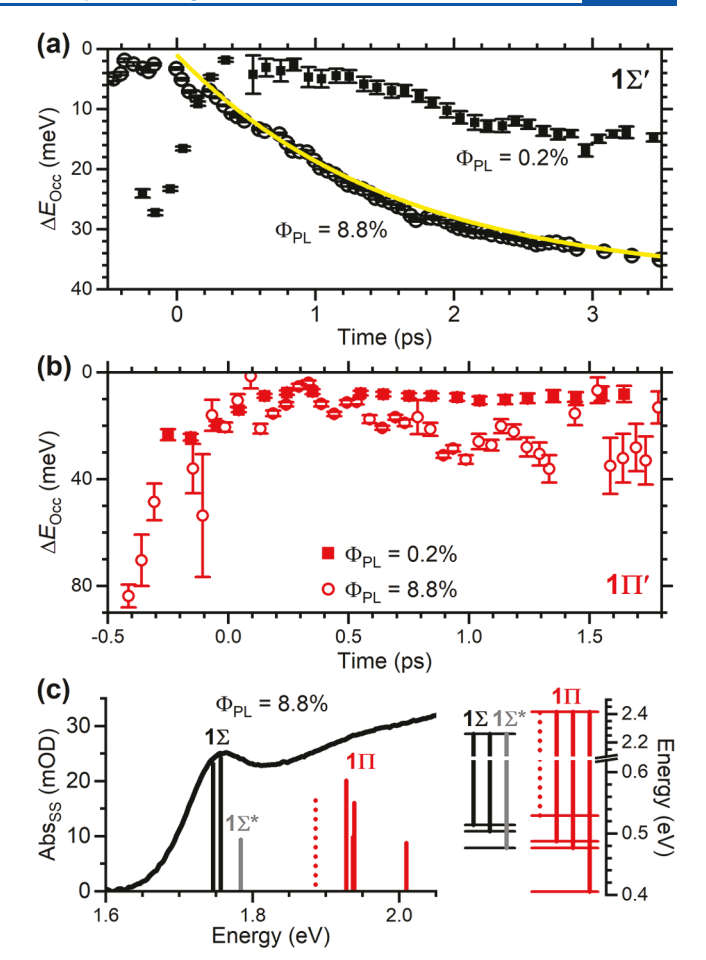


Figure 5. (a and b) Time-dependence of the energies of the $1\Sigma'$ and $1\Pi'$ occupancy features of the $\Phi_{PL}=0.2\%$ and 8.8% WZ CdTe QW samples, filled squares and open circles, respectively. The yellow line is a single-exponential fit, $\tau=1.6(1)$ ps, of the growth of the $1\Sigma'$ feature for the high-quality sample. The vertical scales are the energies of the occupancy features below the 1Σ and 1Π features in the $Abs_{SS}(E)$ spectra. (c) $Abs_{SS}(E)$ spectrum of the high-quality $\Phi_{PL}=8.8\%$ WZ CdTe QWs. Tics indicate the strongest calculated transitions 32,33 with the states accessed by each shown on the energy state diagram.

The temporal profile of $\Delta E_{\rm Occ}(t)$ of the $1\Sigma'$ feature of the Φ_{PL} = 8.8% sample, open circles in Figure 5a, is markedly different than that for the low-quality QWs. There is a smooth, nearly single-exponential shift of $\Delta E_{\rm Occ}(t)$ from ~0 meV to the long-time value of 35.9(3) meV, which is significantly larger than the average shift obtained in the QSR model fitting, $\langle \Delta E_{\rm OSR}(t) \rangle$ = 21 meV. This discrepancy illustrates shortcomings of the simple QSR model implemented and that higher-level calculations of the state-specific QSR are needed to better quantify the photoinduced state shifting. Nevertheless, the larger QSR of the $1\Sigma'$ occupancy features measured for the Φ_{PL} = 8.8% sample in comparison to the Φ_{PL} = 0.2% sample is attributed to the larger fraction of carriers, especially holes, that have relaxed to the band-edge states. The excitation fluence of $\sim 4 \mu J \text{ cm}^{-2} \text{ pulse}^{-1} \text{ used in}$ these measurements results in the generation of ~ 10 electron/ hole pairs μm^{-1} pulse⁻¹. The PL efficiency spectrum for these Φ_{PL} = 8.8% QWs, Figure S4 in Supporting Information, indicates that a fraction of the carriers do become trapped while relaxing to the band-edge states. If the value of Φ_{PL} = 8.8% is attributed solely to hole trapping, then \sim 0.88 holes

 μm^{-1} pulse⁻¹ in the band-edge states radiatively recombine with electrons. This hole density is nearly 6× larger for the Φ_{PL} = 8.8% QWs than for the Φ_{PL} = 0.2% QWs.

These shifting energies are associated with the magnitude of the QSR and changes in the effective masses of the photoexcited carriers in the QWs. The bulk band gap of WZ CdTe, ~1.50 eV,71 and the use of the effective mass approximation and the assumption of a particle-in-a-cylinder dependence for the quantum confinement of the lowest energy $1\Sigma'$ feature ⁷² is used to estimate the change of the effective mass, m^* , associated with the QSR. This approximation ignores that the bottom of the band and thus the bottom of the confinement potential also shifts with a change in m^* . The long-time energy of the $1\Sigma'$ feature of the lower-quality QWs is 1.687 or 0.187 eV above the bulk band-edge energy. Taking the ratio of this energy shift to that of the 1Σ feature in the $Abs_{SS}(E)$ spectrum above the band gap energy, 0.203 eV, reveals the m^* in these QWs increases by $\sim 9\%$ after the carriers have reached the band-edge states. We infer that this change in m^* is largely dictated by electrons, as the low $\Phi_{\rm PL}$ value of this sample is associated with the trapping of holes. The long-time shift of the $1\Sigma'$ feature of the high-quality QWs is 0.211 eV, and the energy of the 1Σ feature is shifted by 0.247 eV above the bulk value. Thus, the value of m^* at long times in these QWs increases by \sim 17%. This significantly larger change in QSR and the value of m^* observed at long times are associated with holes also relaxing in the band-edge states.

The temporal profile of $\Delta E_{\rm Occ}(t)$ of the $1\Sigma'$ feature of the high-quality Φ_{PL} = 8.8% WZ CdTe QWs was fit to a singleexponential function with a time constant of $\tau = 1.6(1)$ ps, as shown by the yellow line in Figure 5a. This time scale is similar to the time it takes for the $1\Sigma'$ occupancy feature of the Φ_{PL} = 0.2% QWs to shift from zero to its long-time value of 15.9(4) meV. This similarity suggests the smooth increase in $\Delta E_{\rm Occ}(t)$ of the $1\Sigma'$ feature of the high-quality QWs tracks with the relaxation dynamics of electrons, either separate electrons or electrons within excitons. The $1\Sigma'$ occupancy feature contains transitions between a few low-lying hole states and only the 1Σ quantum-confinement state in the CB, as indicated in Figure 5c. The energetic proximity of the hole states likely results in state mixing, and consequently, they may experience similar QSR. We conclude that these transitions likely contribute nearly the same intensities and energy shifts to the $1\Sigma'$ occupancy feature of the Φ_{PL} = 8.8% QWs, thereby representing a frequency modulation in the energy of this feature.

The Stokes shift of the PL maximum below the lowestenergy $Abs_{SS}(E)$ feature is sometimes attributed to the fine structure of the hole states of the semiconductor NP. 73,74 Calculations of the fine structure indicate the resultant transitions are typically $<\!20$ meV with a dependence on size and dimensionality. Excitation will access all of these transitions, and emission will occur from a quasi-equilibrium of carriers in these states after the electrons and holes relax into the band-edge states. The predicted fine structure of the hole states in one-dimensional QWs indicates the lowest-energy transitions are optically bright. 63-66 Thus, the carrier populations relax to and emit from these lowest-energy states. As these experiments were performed at room temperature, we conclude that there is carrier population in most of these hole states, and the fine structure will not contribute significantly to the Stokes shift observed. A spontaneous emission event in a CdTe QW that occurs when low-excitation fluences are used is

attributed to the recombination of one electron and one hole, each in a QSR-shifted band-edge state, bound together as a one-dimensional exciton. Consequently, a major contribution of the Stokes shift of the steady-state PL feature from the lowest-energy 1Σ steady-state absorption feature is attributed to the QSR of these band-edge states at long times.

The 18 and 49 meV Stokes shifts of the Φ_{PL} = 0.2% and 8.8% WZ CdTe QWs, shown in Figure 2, are \sim 13% and \sim 36% larger than the long-time QSR shifts of the $1\Sigma'$ occupancy feature, 15.9 and 35.9 meV. There are several reasons the Stokes shifts observed are larger than the QSR of the bandedge states. The excitons have one free dimension for translational motion, and the excitons in these experiments will have a room-temperature Boltzmann distribution of energies. The $1\Sigma'$ occupancy feature obtained from the TA data will mimic this distribution. In contrast, momentum conservation constraints dictate that only those excitons with nearly zero translational momentum and thus the lowestenergy excitons in the QWs can radiatively combine. 10 In addition, the presence of shallow trap states or variations in the potential-energy landscape along the length of the WZ CdTe QWs, even those with high Φ_{PL} values, can localize excitons and facilitate the radiative recombination of those excitons in the low-energy range of the thermal distribution. The presence of phonons in the room-temperature QWs as well as phononassisted recombination would also shift the PL to lower energies than the shifted band-edge quantum-confinement states.

The energies and temporal trends of the $1\Pi'$ occupancy features measured for the $\Phi_{PL}=8.8\%$ and $\Phi_{PL}=0.2\%$ QWs are also notably different. The energies of the $1\Pi'$ occupancy feature for the high-quality QWs, open circles in Figure 5b, are initially >80 meV below the energy of the 1Π steady-state absorption feature. This feature promptly shifts to ~ 0 meV during the excitation pulse, and then increases to 33 meV on a slower time scale, ~ 1.5 ps, where it remains. The energetic shifts of the $1\Pi'$ occupancy feature for the lower-quality QWs begin near 20 meV and quickly stabilize near ~ 9 meV. We attribute these differences to more than just the QSR of the $1\Pi'$ occupancy feature.

The hole states contributing to the $1\Pi'$ occupancy feature span a wider energy range, >120 meV, than those within the $1\Sigma'$ feature, <20 meV. Furthermore, the transition from the band-edge hole state to the $1\Pi'$ state, indicated by a dotted line in Figure 5c, is on the lower-energy side of the $1\Pi'$ feature. These energetics lead us to conclude that the large $\Delta E_{\rm Occ}(t)$ values observed near t = 0 ps for the $1\Pi'$ occupancy feature of the high-quality Φ_{PL} = 8.8% WZ CdTe QWs are associated with holes that were not bound within 1D excitons that relaxed quickly to the band-edge state in the VB. The relaxation time of the excitons is slower, as will be discussed, and the occupancies associated with excitons dominate $\Delta E_{\rm Occ}(t)$ for t >0 ps. As a result, the centroid of the $1\Pi'$ occupancy feature quickly moves from larger shifts, to near 0 meV, and eventually to the long-time value, ~33 meV. So, while there are likely contributions from a QSR-induced energetic shifting of this $1\Pi'$ occupancy feature (frequency modulation), there are also amplitude modulations caused by the lower-energy transition contributing at shorter times and the higher-energy transitions dominating at longer times. Since most of the holes were trapped during relaxation or once they reach the band-edge states in the lower-quality Φ_{PL} = 0.2% WZ CdTe QWs, this

large $\Delta E_{\rm Occ}(t)$ at short time was not observed, red filled squares in Figure 5b.

The identification of clear trends and differences in the energies of the other occupancy features for these CdTe QW samples is difficult. The time dependences of the QSR shifts of each occupancy feature, $\Delta E_{\rm Occ}(t)$, are included in Figures S10 and S11 in Supporting Information. All of the features shift to energies lower than those identified in the Abs_{SS}(E) spectra, especially at short times after excitation. The magnitudes of the feature shifting are larger for the high-quality sample than for the lower quality sample, and we attribute those differences to there being more carriers remaining within the high-quality QWs than in the lower-quality QWs.

Following the results reported on the renormalization of the band-edge states in monolayer ${\rm MoS_2},^{34,35}$ the photoexcitation changes the carrier screening experienced by each electron and hole in the WZ CdTe QWs. The screening for separate carriers and excitons will likely differ, and contributions from both are expected in both samples of the CdTe QWs as their $\Phi_{\rm PL}$ values are not unity. The QSR of all of the quantum-confinement states to lower energies indicates the effective masses of the carriers and excitons are larger in the excited WZ CdTe QWs than in the unexcited QWs.

Intraband Relaxation Dynamics. The IRD of the photoexcited carriers in the $\Phi_{\rm PL}$ = 0.2% and 8.8% WZ CdTe QWs give rise to the temporal profiles of the occupancy features plotted in Figure 6 as filled squares and open circles, respectively. Each point in the plots represents the integrated intensity of the Gaussian peak associated with that occupancy feature at a given time. The temporal profile of each feature was fit using exponential rises and decays convoluted with a 0.230 ps Gaussian instrument response function. The rise and decay time constants, $\tau_{r^{\prime}}$ and $\tau_{d^{\prime}}$ for each occupancy feature in both samples are listed in Table 1.

The carrier occupancies in the high-energy $1\Phi'/2\Pi'/1\Gamma'$ features, Figure 6a, have extremely short rise times, <0.2 and 0.26(1) ps for the $\Phi_{PL}=0.2\%$ and 8.8% QWs, respectively. Excitation in these TA experiments was ~350 and ~250 meV above the corresponding $1\Phi/2\Pi/1\Gamma$ steady-state absorption features for the $\Phi_{PL}=0.2\%$ and 8.8% QW samples. Thus, even though the carriers were excited to slightly higher energies in the lower-quality QWs, the carriers occupied these quantum-confinement states on shorter time scales than those in the high-quality QWs. The rise times for the occupancy features increase with decreasing energies for both samples, and there is a trend of slower rise times for the same occupancy features in the high-quality QWs in comparison to those in the lower-quality QWs.

A sum of exponential decays was needed to fit the $1\Sigma'$ and $1\Sigma^{*'}$ occupancy profiles for both samples. The average decay constant for the $\Phi_{PL}=0.2\%$ QWs was only 232(6) ps, which is consistent with the low quantum yield. The decay profile of the $\Phi_{PL}=8.8\%$ QWs is much longer, as expected for the higher quantum yield of this sample, with the most significant contribution exceeding the temporal delay limit of the TA measurements of 7000 ps. Note the lifetimes of 1D excitons in high-quality, $\Phi_{PL} \geq 4\%$ WZ CdTe QWs were measured to be $>\!200$ ns. 10

The growth of the $1\Sigma'$ occupancy feature of the lower-quality $\Phi_{PL}=0.2\%$ QWs has two rise-time components, as reported previously.³³ The instrument-limited component was attributed to the small fraction of holes that were not trapped before reaching the low-energy states, and the slower

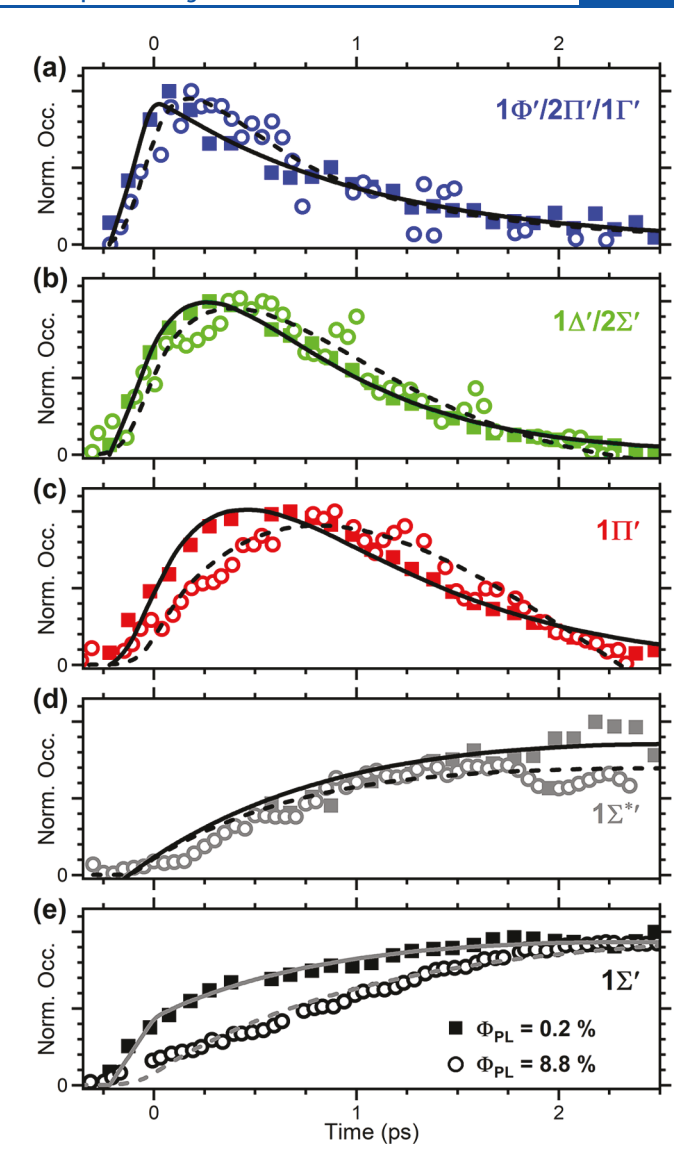


Figure 6. Temporal profiles of the occupancy features for the lower-quality Φ_{PL} = 0.2% (solid squares) and high-quality Φ_{PL} = 8.8% (open circles) WZ CdTe QWs. The solid and dashed lines are fits of the temporal profiles of the Φ_{PL} = 0.2% and 8.8% samples with the parameters provided in Table 1.

Table 1. Rise, τ_r , and Decay, τ_d , Time Constants of the Occupancy Features Containing the Indicated Quantum-Confinement States of the Lower-Quality $\Phi_{PL}=0.2\%$ and High-Quality $\Phi_{PL}=8.8\%$ WZ CdTe QWs

	$\Phi_{\rm PL} = 0.2\%^a$		$\Phi_{\rm PL}=8.8\%$	
Quantum States	$\tau_{\rm r}~({\rm ps})$	$\tau_{\rm d}~({\rm ps})$	$\tau_{\rm r}~({\rm ps})$	$\tau_{\rm d}~({\rm ps})$
$1\Phi'/2\Pi'/1\Gamma'$	<0.2	1.03(6)	0.26(1)	1.1(3)
$1\Delta'/2\Sigma'$	0.29(1)	0.62(2)	0.80(9)	0.8(1)
$1\Pi'$	0.50(2)	0.65(2)	1.5(3)	1.7(3)
$1\Sigma^{*'}$	1.3(3)	$230(30)^{b}$	1.78(5)	>7000°
$1\Sigma'$	< 0.2 and $1.10(2)^d$	$232(6)^{b}$	1.90(4)	>7000°

^aThese data and fitting for the as-synthesized WZ CdTe QWs are the same as reported in ref 33. ^bThese decay profiles are multiexponential, and the values given represent the average lifetimes, $\langle \tau_{\rm d} \rangle$. ^cThe decay time constant is longer than the limit of the instrument measurement time, 7000 ps. ^dThis rise was best fit with one component within the instrument response and a second, longer time constant.

component, 1.10 ps, was associated with electrons relaxing into the lowest-energy, $1\Sigma'$ quantum-confinement state in the CB. The low Φ_{PL} of these QWs indicates that many of the carriers, especially the holes, became trapped either during relaxation to the band-edge states or after reaching them. Although, some of the photoexcited electron—hole pairs may have relaxed as excitons in the lower-quality QWs, most of the carriers likely separated and did not radiatively recombine. Based on the calculated transition energies 33 each photoexcited electron was created at $\sim\!0.60$ eV above the $1\Sigma'$ electron state in the CB. A relaxation time of 1.10 ps yields an electron relaxation rate of $\sim\!0.60$ eV ps $^{-1}$. Each photoexcited hole was created at $\sim\!0.42$ eV from the lowest-energy QSR-shifted hole states. The ultrashort relaxation time of <0.200 ps yields a hole relaxation rate of >2.0 eV ps $^{-1}$.

In contrast, the $1\Sigma'$ occupancy feature of the high-quality WZ CdTe QWs has only one identifiable rise time, and it is notably longer, 1.90 ps, than measured for the lower-quality QWs. As the transitions within the $1\Sigma'$, $1\Sigma^{*\prime}$, and $1\Sigma'$ -VB-1' occupancy features have the electron $1\Sigma'$ quantum-confinement state in common, an identical constant in the profiles of these features should be associated with the IRD of electrons to the band edge. The rise of the $1\Sigma'$ occupancy feature is similar to that of the $1\Sigma'$ -VB-1' feature; see Figure S11 in Supporting Information. The rise of the $1\Sigma^{*'}$ occupancy feature is marginally faster than that of the $1\Sigma'$ feature, and this difference may be due to holes relaxing through the slightly excited, quantum-confinement state associated with the $1\Sigma^{*'}$ transition that would be occupied before the lower-energy states. Note the rise times of the $1\Sigma'$ feature in the occupancy data for both samples is significantly longer than the rise times of the 1Σ band-edge bleach features present in the TA data. These differences emphasize the need to account for QSR when attempting to identify the time scales for carrier relaxation using pump-probe spectral methods, either TA or two-dimensional electronic spectroscopy.

A high quantum yield, Φ_{PL} = 8.8%, measured using low excitation fluences indicates that the PL was from geminate radiative recombination of photoexcited electron-hole pairs. That coupled with a single-exponential rise of the $1\Sigma'$ occupancy feature, instead of a double-exponential rise, leads to the conclusion that a significant fraction of the photoexcited electrons and holes, ~ 0.88 electron—hole pairs μm^{-1} pulse⁻¹, relaxed to the band-edge states as bound 1D excitons in the high-quality WZ CdTe QWs. As such, the time scales for IRD to the band-edge states are the same for the electrons and holes, and the carrier relaxation rates must be different. Each electron was promoted to ~ 0.63 eV above the $1\Sigma'$ electron state in the CB. A relaxation time of 1.90 ps indicates that the electron relaxation rate is ~ 0.33 eV ps⁻¹ in the high-quality QWs. Each photoexcited hole was created at ~0.44 eV from the lowest-energy QSR-shifted hole states. The same relaxation time yields a hole relaxation rate of ~ 0.23 eV ps⁻¹ in these QWs.

The picture for the relaxation of the electron—hole pairs in the high-quality $\Phi_{PL}=8.8\%$ WZ CdTe QWs shows that a significant fraction of these carriers remained bound as 1D excitons while relaxing to the band-edge states and until they radiatively recombined. In contrast, there were many trap states in the lower-quality $\Phi_{PL}=0.2\%$ QWs, and most of the carriers did not remain bound as 1D excitons. The shorter rise time of the $1\Sigma'$ feature in these QWs indicates many carriers were trapped before reaching the band-edge states. From a

simple kinetics perspective, the relaxation rate of a carrier to the band-edge, k_{Tot} is dictated by all pathways present. If there are parallel processes present, such as phonon relaxation to lower energy states, with a rate of $k_{\rm rel}$, and delocalization to surface traps, with a rate of k_{trap} , then the total rate for relaxation is $k_{\rm Tot}$ = $k_{\rm rel}$ + $k_{\rm trap}$. The rise time of the occupancy in the band-edge states, $\tau_{\rm r} = \hat{k}_{\rm Tot}^{-1}$, would then be shorter when there are many trap states competing with intraband relaxation. The dynamics and kinetics were more complicated than this in the QWs as many quantum-confinement states and dissimilar trap states were likely sampled as the carriers relaxed to the band-edge states. The contrasting relaxation times for the $\Phi_{
m PL}$ = 8.8% and 0.2% QWs give direct evidence of nonunity relaxation efficiencies of carriers to the band-edge states that depend on the initial energy at which the carriers were excited. Furthermore, this supports the conclusions drawn that there is an excitation-energy dependence of the Φ_{PL} in some NPs, especially if the Φ_{PL} values are not high.

There are contrasting results reported in the literature on the efficiency of the intraband relaxation of photoexcited carriers to the band-edge states in semiconductor NPs; numerous types of NPs exhibited a dependence of the Φ_{PL} on excitation energy, $^{69,70,82-89}$ but other studies indicated some NPs exhibit no dependence of Φ_{PL} on excitation energy. To determine the roles of excitation energy, surface traps, defects, energy-coupling mechanisms, and densities of states in the dynamics and energetics of electrons, holes, and excitons in NPs, accurate characterization of the state-to-state IRD of photogenerated charge carriers in them remains a high priority. As illustrated previously, 32,33 it is essential to account for the contributions of QSR in order to accurately identify the IRD and energetics of the photoexcited carriers.

CONCLUSIONS

TA spectroscopy experiments were performed on two samples of WZ CdTe QWs, one with Φ_{PL} = 0.2% and one with Φ_{PL} = 8.8%. A simple model³² was used to separate contributions from QSR of the different features and carrier occupancies. Larger QSR was observed for the high-quality $\Phi_{PL} = 8.8\%$ QWs, and this is attributed to the presence of a significant fraction of the photoexcited electrons and holes remaining in the QWs. The QSR does depend on the specific states occupied by the carriers, and each changes as the carriers relax. The time scales for intraband relaxation of the photoexcited electrons and holes are longer in the Φ_{PL} = 8.8% QWs, and the data indicate the carriers relax as excitons. The shorter time for the lower-quality Φ_{PL} = 0.2% QWs is attributed to the presence of traps that were accessed during relaxation, thereby confirming that there is an excitation-energy dependence of the PL efficiency on excitation energy in these QWs.

The results presented indicate the importance of accounting for QSR when analyzing TA data and characterizing the IRD in semiconductor NPs that have measurable quantum-confinement effects. High-level calculations probing the QSR of the different electron and hole quantum-confinement states would prove to be invaluable for further interpreting the interactions and dynamics within semiconductor NPs.

ASSOCIATED CONTENT

Supporting Information

The Supporting Information is available free of charge at https://pubs.acs.org/doi/10.1021/acs.jpcc.3c05672.

TEM image of as-synthesized WZ CdTe QWs, steadystate and TA data, extraction of occupancy contributions using the QSR model, exponential fitting of carrier occupancies, comparison of TA temporal profiles with occupancy profiles, as well as additional data and figures are included. (PDF)

AUTHOR INFORMATION

Corresponding Author

Richard A. Loomis — Department of Chemistry and Institute of Materials Science and Engineering, Washington University in Saint Louis, Saint Louis, Missouri 63130, United States; orcid.org/0000-0002-3172-6336; Email: loomis@wustl.edu

Authors

Jie Chen – Department of Chemistry and Institute of Materials Science and Engineering, Washington University in Saint Louis, Saint Louis, Missouri 63130, United States; orcid.org/0000-0002-6591-3412

William M. Sanderson – Department of Chemistry and Institute of Materials Science and Engineering, Washington University in Saint Louis, Saint Louis, Missouri 63130, United States

Complete contact information is available at: https://pubs.acs.org/10.1021/acs.jpcc.3c05672

Notes

The authors declare no competing financial interest.

ACKNOWLEDGMENTS

This work was supported by the NSF under grant DMR-1905751. The authors acknowledge F. Wang and W. E. Buhro for their assistance in the synthesis of the samples used in this study and continuous discussions regarding the results.

■ REFERENCES

- (1) Leschkies, K. S.; Divakar, R.; Basu, J.; Enache-Pommer, E.; Boercker, J. E.; Carter, C. B.; Kortshagen, U. R.; Norris, D. J.; Aydil, E. S. Photosensitization of ZnO Nanowires with CdSe Quantum Dots for Photovoltaic Devices. *Nano Lett.* **2007**, *7*, 1793–1798.
- (2) Kapon, E.; Simhony, S.; Bhat, R.; Hwang, D. M. Single Quantum Wire Semiconductor Lasers. *Appl. Phys. Lett.* **1989**, *55*, 2715–2717.
- (3) Vaillancourt, J.; Vasinajindakaw, P.; Lu, X. A High Operating Temperature (Hot) Middle Wave Infrared (MWIR) Quantum-Dot Photodetector. *Opt. Photon. Lett.* **2011**, *04*, 57–61.
- (4) Howarth, M.; Liu, W.; Puthenveetil, S.; Zheng, Y.; Marshall, L. F.; Schmidt, M. M.; Wittrup, K. D.; Bawendi, M. G.; Ting, A. Y. Monovalent, Reduced-Size Quantum Dots for Imaging Receptors on Living Cells. *Nat. Methods* **2008**, *5*, 397–399.
- (5) Law, M.; Greene, L. E.; Johnson, J. C.; Saykally, R.; Yang, P. Nanowire Dye-Sensitized Solar Cells. *Nature* **2005**, *4*, 455–459.
- (6) Utterback, J. K.; Grennell, A. N.; Wilker, M. B.; Pearce, O. M.; Eaves, J. D.; Dukovic, G. Observation of Trapped-Hole Diffusion on the Surfaces of CdS Nanorods. *Nat. Chem.* **2016**, *8*, 1061–1066.
- (7) Wang, F.; Yu, H.; Li, J.; Hang, Q.; Zemlyanov, D.; Gibbons, P. C.; Wang, L.-W.; Janes, D. B.; Buhro, W. E. Spectroscopic Properties of Colloidal Indium Phosphide Quantum Wires. *J. Am. Chem. Soc.* **2007**, *129*, 14327–14335.
- (8) Kuno, M. An Overview of Solution-Based Semiconductor Nanowires: Synthesis and Optical Studies. *Phys. Chem. Chem. Phys.* **2008**, *10*, 620–639.
- (9) Glennon, J. J.; Tang, R.; Buhro, W. E.; Loomis, R. A. Synchronous Photoluminescence Intermittency (Blinking) Along

- Whole Semiconductor Quantum Wires. Nano Lett. 2007, 7, 3290-3295.
- (10) Sanderson, W. M.; Wang, F.; Buhro, W. E.; Loomis, R. A. Long-Lived 1D Excitons in Bright CdTe Quantum Wires. *J. Phys. Chem. C* 2019, 123, 3144–3151.
- (11) Liu, Y.-H.; Wang, F.; Hoy, J.; Wayman, V. L.; Steinberg, L. K.; Loomis, R. A.; Buhro, W. E. Bright Core—Shell Semiconductor Quantum Wires. J. Am. Chem. Soc. 2012, 134, 18797—18803.
- (12) McArthur, E. A.; Morris-Cohen, A. J.; Knowles, K. E.; Weiss, E. A. Charge Carrier Resolved Relaxation of the First Excitonic State in CdSe Quantum Dots Probed with near-Infrared Transient Absorption Spectroscopy. *J. Phys. Chem. B* **2010**, *114*, 14514–14520.
- (13) Vietmeyer, F.; Chatterjee, R.; McDonald, M. P.; Kuno, M. Concerted Single-Nanowire Absorption and Emission Spectroscopy: Explaining the Origin of the Size-Dependent Stokes Shift in Single Cadmium Selenide Nanowires. *Phys. Rev. B* **2015**, *91*, No. 085422.
- (14) Morgan, D. P.; Maddux, C. J. A.; Kelley, D. F. Transient Absorption Spectroscopy of CdSe Nanoplatelets. *J. Phys. Chem. C* **2018**, 122, 23772–23779.
- (15) Klimov, V.; Hunsche, S.; Kurz, H. Biexciton Effects in Femtosecond Nonlinear Transmission of Semiconductor Quantum Dots. *Phys. Rev. B* **1994**, *50*, 8110–8113.
- (16) Klimov, V. I.; McBranch, D. W.; Leatherdale, C. A.; Bawendi, M. G. Electron and Hole Relaxation Pathways in Semiconductor Quantum Dots. *Phys. Rev. B* **1999**, *60*, 13740–13749.
- (17) Hu, Y. Z.; Koch, S. W.; Lindberg, M.; Peyghambarian, N.; Pollock, E. L.; Abraham, F. F. Biexcitons in Semiconductor Quantum Dots. *Phys. Rev. Lett.* **1990**, *64*, 1805–1807.
- (18) Hu, Y. Z.; Lindberg, M.; Koch, S. W. Theory of Optically Excited Intrinsic Semiconductor Quantum Dots. *Phys. Rev. B* **1990**, 42, 1713–1723.
- (19) Park, S. H.; Morgan, R. A.; Hu, Y. Z.; Lindberg, M.; Koch, S. W.; Peyghambarian, N. Nonlinear Optical Properties of Quantum-Confined CdSe Microcrystallites. *J. Opt. Soc. Am. B* **1990**, *7*, 2097–2105.
- (20) Kang, K. I.; Kepner, A. D.; Gaponenko, S. V.; Koch, S. W.; Hu, Y. Z.; Peyghambarian, N. Confinement-Enhanced Biexciton Binding Energy in Semiconductor Quantum Dots. *Phys. Rev. B* **1993**, *48*, 15449–15452.
- (21) Sewall, S. L.; Cooney, R. R.; Anderson, K. E. H.; Dias, E. A.; Kambhampati, P. State-to-State Exciton Dynamics in Semiconductor Quantum Dots. *Phys. Rev. B* **2006**, *74*, 235328.
- (22) Klimov, V. I. Properties of Multiexcitons in Semiconductor Nanocrystals. *Annu. Rev. Phys. Chem.* **2007**, *58*, 635–673.
- (23) Yan, Y.; Chen, G.; Van Patten, P. G. Ultrafast Exciton Dynamics in CdTe Nanocrystals and Core/Shell CdTe/CdS Nanocrystals. *J. Phys. Chem. C* **2011**, *115*, 22717–22728.
- (24) Schnitzenbaumer, K. J.; Labrador, T.; Dukovic, G. Impact of Chalcogenide Ligands on Excited State Dynamics in CdSe Quantum Dots. J. Phys. Chem. C 2015, 119, 13314–13324.
- (25) Li, Q.; Lian, T. A Model for Optical Gain in Colloidal Nanoplatelets. *Chem. Sci.* **2018**, *9*, 728–734.
- (26) Vashishta, P.; Kalia, R. K. Universal Behavior of Exchange-Correlation Energy in Electron-Hole Liquid. *Phys. Rev. B* **1982**, 25, 6492–6495.
- (27) Wegscheider, W.; Pfeiffer, L. N.; Dignam, M. M.; Pinczuk, A.; West, K. W.; McCall, S. L.; Hull, R. Lasing from Excitons in Quantum Wires. *Phys. Rev. Lett.* **1993**, *71*, 4071–4074.
- (28) Cingolani, R.; Rinaldi, R.; Ferrara, M.; La Rocca, G. C.; Lage, H.; Heitmann, D.; Ploog, K.; Kalt, H. Band-Gap Renormalization in Quantum Wires. *Phys. Rev. B* **1993**, *48*, 14331–14337.
- (29) Wang, K. H.; Bayer, M.; Forchel, A.; Ils, P.; Benner, S.; Haug, H.; Pagnod-Rossiaux, P.; Goldstein, L. Subband Renormalization in Dense Electron-Hole Plasmas in In_{0.53}Ga_{0.47}As/InP Quantum Wires. *Phys. Rev. B* **1996**, *53*, R10505.
- (30) Titova, L. V.; Hoang, T. B.; Yarrison-Rice, J. M.; Jackson, H. E.; Kim, Y.; Joyce, H. J.; Gao, Q.; Tan, H. H.; Jagadish, C.; Zhang, X.; et al. Dynamics of Strongly Degenerate Electron-Hole Plasmas and Excitons in Single InP Nanowires. *Nano Lett.* **2007**, *7*, 3383–3387.

- (31) Perera, S.; Fickenscher, M. A.; Jackson, H. E.; Smith, L. M.; Yarrison-Rice, J. M.; Joyce, H. J.; Gao, Q.; Tan, H. H.; Jagadish, C.; Zhang, X.; Zou, J.; et al. Nearly Intrinsic Exciton Lifetimes in Single Twin-Free GaAs/AlGaAs Core-Shell Nanowire Heterostructures. *Appl. Phys. Lett.* **2008**, *93*, No. 053110.
- (32) Sanderson, W. M.; Schrier, J.; Loomis, R. A. Photo-Induced State Shifting in 1D Semiconductor Quantum Wires. *J. Phys. Chem. C* **2020**, *124*, 16702–16713.
- (33) Sanderson, W. M.; Schrier, J.; Wang, F.; Buhro, W. E.; Loomis, R. A. Intraband Relaxation Dynamics of Charge Carriers within CdTe Quantum Wires. *J. Phys. Chem. Lett.* **2020**, *11*, 4901–4910.
- (34) Lin, Y.; Chan, Y.-h.; Lee, W.; Lu, L.-S.; Li, Z.; Chang, W.-H.; Shih, C.-K.; Kaindl, R. A.; Louie, S. G.; Lanzara, A. In Exciton-Driven Ultrafast Enhancement of Quasiparticle Bandgap and Effective Mass in Monolayer MoS2, Conference on Lasers and Electro-Optics, San Jose, California, 2022/05/15; Optica Publishing Group: San Jose, CA, 2022; p FTu4B.1.
- (35) Lin, Y.; Chan, Y.-h.; Lee, W.; Lu, L.-S.; Li, Z.; Chang, W.-H.; Shih, C.-K.; Kaindl, R. A.; Louie, S. G.; Lanzara, A. Exciton-Driven Renormalization of Quasiparticle Band Structure in Monolayer MoS₂. *Phys. Rev. B* **2022**, *106*, L081117.
- (36) Liu, F. Time- and Angle-Resolved Photoemission Spectroscopy (TR-ARPES) of TMDC Monolayers and Bilayers. *Chem. Sci.* **2023**, 14, 736–750.
- (37) Pogna, E. A. A.; Marsili, M.; De Fazio, D.; Dal Conte, S.; Manzoni, C.; Sangalli, D.; Yoon, D.; Lombardo, A.; Ferrari, A. C.; Marini, A.; et al. Photo-Induced Bandgap Renormalization Governs the Ultrafast Response of Single-Layer MoS₂. ACS Nano **2016**, 10, 1182–1188.
- (38) Cunningham, P. D.; Hanbicki, A. T.; McCreary, K. M.; Jonker, B. T. Photoinduced Bandgap Renormalization and Exciton Binding Energy Reduction in WS₂. ACS Nano **2017**, 11, 12601–12608.
- (39) Wood, R. E.; Lloyd, L. T.; Mujid, F.; Wang, L.; Allodi, M. A.; Gao, H.; Mazuski, R.; Ting, P.-C.; Xie, S.; Park, J.; et al. Evidence for the Dominance of Carrier-Induced Band Gap Renormalization over Biexciton Formation in Cryogenic Ultrafast Experiments on MoS₂ Monolayers. J. Phys. Chem. Lett. **2020**, 11, 2658–2666.
- (40) Smejkal, V.; Libisch, F.; Molina-Sanchez, A.; Trovatello, C.; Wirtz, L.; Marini, A. Time-Dependent Screening Explains the Ultrafast Excitonic Signal Rise in 2D Semiconductors. *ACS Nano* **2021**, *15*, 1179–1185.
- (41) Lloyd, L. T.; Wood, R. E.; Mujid, F.; Sohoni, S.; Ji, K. L.; Ting, P.-C.; Higgins, J. S.; Park, J.; Engel, G. S. Sub-10 fs Intervalley Exciton Coupling in Monolayer MoS₂ Revealed by Helicity-Resolved Two-Dimensional Electronic Spectroscopy. *ACS Nano* **2021**, *15*, 10253–10263.
- (42) Dingle, R. Confined Carrier Quantum States in Ultrathin Semiconductor Heterostructures. *Festkoerperprobleme* **1975**, *15*, 21–48
- (43) Yoffe, A. D. Low-Dimensional Systems: Quantum Size Effects and Electronic Properties of Semiconductor Microcrystallites (Zero-Dimensional Systems) and Some Quasi-Two-Dimensional Systems. *Adv. Phys.* **1993**, 42, 173–266.
- (44) Adamowski, J. Formation of Fröhlich Bipolarons. *Phys. Rev. B* **1989**, 39, 3649–3652.
- (45) Feng, D. H.; Xu, Z. Z.; Jia, T. Q.; Li, X. X.; Li, C. B.; Sun, H. Y.; Xu, S. Z. Polaronic Correction to the First Excited Electronic Energy Level in Ananisotropic Semiconductor Quantum Dot. *Eur. Phys. J. B* **2005**, *44*, 15–20.
- (46) Sellami, K.; Jaziri, S. Exciton-Polaron in a CdSe Quantum Dot under an Applied Magnetic Field. *Physica E Low Dimens. Syst. Nanostruct.* **2005**, *26*, 143–148.
- (47) Trushin, M.; Sarkar, S.; Mathew, S.; Goswami, S.; Sahoo, P.; Wang, Y.; Yang, J.; Li, W.; MacManus-Driscoll, J. L.; Chhowalla, M.; et al. Evidence of Rotational Fröhlich Coupling in Polaronic Trions. *Phys. Rev. Lett.* **2020**, *125*, No. 086803.
- (48) Denning, E. V.; Iles-Smith, J.; Gregersen, N.; Mork, J. Phonon Effects in Quantum Dot Single-Photon Sources. *Opt. Mater. Express* **2020**, *10*, 222–239.

- (49) Kelley, A. M. Electron—Phonon Coupling in CdSe Nanocrystals. J. Phys. Chem. Lett. 2010, 1, 1296—1300.
- (50) Kelley, A. M. Electron-Phonon Coupling in CdSe Nanocrystals from an Atomistic Phonon Model. ACS Nano 2011, 5, 5254-5262.
- (51) Kelley, A. M.; Dai, Q.; Jiang, Z.-j.; Baker, J. A.; Kelley, D. F. Resonance Raman Spectra of Wurtzite and Zincblende CdSe Nanocrystals. *Chem. Phys.* **2013**, 422, 272–276.
- (52) Lin, C.; Gong, K.; Kelley, D. F.; Kelley, A. M. Electron—Phonon Coupling in CdSe/CdS Core/Shell Quantum Dots. *ACS Nano* **2015**, *9*, 8131–8141.
- (53) Boldt, K. Raman Spectroscopy of Colloidal Semiconductor Nanocrystals. *Nano Futures* **2022**, *6*, No. 012003.
- (54) Sagar, D. M.; Cooney, R. R.; Sewall, S. L.; Dias, E. A.; Barsan, M. M.; Butler, I. S.; Kambhampati, P. Size Dependent, State-Resolved Studies of Exciton-Phonon Couplings in Strongly Confined Semi-conductor Quantum Dots. *Phys. Rev. B* **2008**, *77*, 235321.
- (55) Sagar, D. M.; Cooney, R. R.; Sewall, S. L.; Kambhampati, P. State-Resolved Exciton—Phonon Couplings in CdSe Semiconductor Quantum Dots. *J. Phys. Chem. C* 2008, *112*, 9124—9127.
- (56) Park, Y.; Limmer, D. T. Renormalization of Excitonic Properties by Polar Phonons. J. Chem. Phys. 2022, 157, 104116.
- (57) Plekhanov, V. G. Chapter 6: Exciton-Phonon Interaction. In *Semiconductors and Semimetals*; Plekhanov, V. G., Ed.; Elsevier: 2001; Vol. 68, pp 135–180.
- (58) Bawendi, M. G.; Wilson, W. L.; Rothberg, L.; Carroll, P. J.; Jedju, T. M.; Steigerwald, M. L.; Brus, L. E. Electronic Structure and Photoexcited-Carrier Dynamics in Nanometer-Size CdSe Clusters. *Phys. Rev. Lett.* **1990**, *65*, 1623–1626.
- (59) Glässl, M.; Vagov, A.; Lüker, S.; Reiter, D. E.; Croitoru, M. D.; Machnikowski, P.; Axt, V. M.; Kuhn, T. Long-Time Dynamics and Stationary Nonequilibrium of an Optically Driven Strongly Confined Quantum Dot Coupled to Phonons. *Phys. Rev. B* **2011**, *84*, 195311.
- (60) Stewart, J. T.; Padilha, L. A.; Qazilbash, M. M.; Pietryga, J. M.; Midgett, A. G.; Luther, J. M.; Beard, M. C.; Nozik, A. J.; Klimov, V. I. Comparison of Carrier Multiplication Yields in PbS and PbSe Nanocrystals: The Role of Competing Energy-Loss Processes. *Nano Lett.* **2012**, *12*, *622*–*628*.
- (61) Sohier, T.; Calandra, M.; Mauri, F. Two-Dimensional Fröhlich Interaction in Transition-Metal Dichalcogenide Monolayers: Theoretical Modeling and First-Principles Calculations. *Phys. Rev. B* **2016**, 94. No. 085415.
- (62) Iaru, C. M.; Brodu, A.; van Hoof, N. J. J.; ter Huurne, S. E. T.; Buhot, J.; Montanarella, F.; Buhbut, S.; Christianen, P. C. M.; Vanmaekelbergh, D.; de Mello Donega, C.; et al. Fröhlich Interaction Dominated by a Single Phonon Mode in CsPbBr₃. *Nat. Commun.* **2021**, *12*, 5844.
- (63) Nirmal, M.; Norris, D. J.; Kuno, M.; Bawendi, M. G.; Efros, A. L.; Rosen, M. Observation of the 'Dark Exciton' in CdSe Quantum Dots. *Phys. Rev. Lett.* **1995**, *75*, 3728–3731.
- (64) Norris, D. J.; Bawendi, M. G. Measurement and Assignment of the Size-Dependent Optical Spectrum in CdSe Quantum Dots. *Phys. Rev. B* **1996**, *53*, 16338–16346.
- (65) Efros, A. L.; Rosen, M. The Electronic Structure of Semiconductor Nanocrystals. *Annu. Rev. Mater. Sci.* **2000**, *30*, 475–521.
- (66) Zhao, Q.; Graf, P. A.; Jones, W. B.; Franceschetti, A.; Li, J.; Wang; Kim, K. Shape Dependence of Band-Edge Exciton Fine Structure in CdSe Nanocrystals. *Nano Lett.* **2007**, *7*, 3274–3280.
- (67) Wang, F.; Buhro, W. E. Crystal-Phase Control by Solution—Solid—Solid Growth of II—VI Quantum Wires. *Nano Lett.* **2016**, *16*, 889–894.
- (68) Wang, F.; Buhro, W. E. An Easy Shortcut Synthesis of Size-Controlled Bismuth Nanoparticles and Their Use in the SLS Growth of High-Quality Colloidal Cadmium Selenide Quantum Wires. *Small* **2010**, *6*, 573–581.
- (69) Hoy, J.; Morrison, P. J.; Steinberg, L. K.; Buhro, W. E.; Loomis, R. A. Excitation Energy Dependence of the Photoluminescence

- Quantum Yields of Core and Core/Shell Quantum Dots. J. Phys. Chem. Lett. 2013, 4, 2053–2060.
- (70) Sanderson, W. M.; Hoy, J.; Morrison, C.; Wang, F.; Wang, Y.; Morrison, P. J.; Buhro, W. E.; Loomis, R. A. Excitation Energy Dependence of Photoluminescence Quantum Yields of Semiconductor Nanoparticles with Varying Dimensionalities. *J. Phys. Chem. Lett.* **2020**, *11*, 3249–3256.
- (71) Sarkar, S.; Pal, S.; Sarkar, P. Electronic Structure and Band Gap Engineering of CdTe Semiconductor Nanowires. *J. Mater. Chem.* **2012**, *22*, 10716–10724.
- (72) Sun, J.; Wang, L. W.; Buhro, W. E. Synthesis of Cadmium Telluride Quantum Wires and the Similarity of Their Effective Band Gaps to Those of Equidiameter Cadmium Telluride Quantum Dots. *J. Am. Chem. Soc.* **2008**, *130*, 7997–8005.
- (73) Palato, S.; Seiler, H.; Baker, H.; Sonnichsen, C.; Brosseau, P.; Kambhampati, P. Investigating the Electronic Structure of Confined Multiexcitons with Nonlinear Spectroscopies. *J. Chem. Phys.* **2020**, *152*, 104710.
- (74) Seiler, H.; Palato, S.; Sonnichsen, C.; Baker, H.; Kambhampati, P. Seeing Multiexcitons through Sample Inhomogeneity: Band-Edge Biexciton Structure in CdSe Nanocrystals Revealed by Two-Dimensional Electronic Spectroscopy. *Nano Lett.* **2018**, *18*, 2999–3006.
- (75) Efros, A. L.; Rosen, M.; Kuno, M.; Nirmal, M.; Norris, D. J.; Bawendi, M. Band-Edge Exciton in Quantum Dots of Semiconductors with a Degenerate Valence Band: Dark and Bright Exciton States. *Phys. Rev. B* **1996**, *54*, 4843–4856.
- (76) Norris, D. J.; Efros, A. L.; Rosen, M.; Bawendi, M. G. Size Dependence of Exciton Fine Structure in CdSe Quantum Dots. *Phys. Rev. B* **1996**, *53*, 16347–16354.
- (77) Crooker, S. A.; Barrick, T.; Hollingsworth, J. A.; Klimov, V. I. Multiple Temperature Regimes of Radiative Decay in CdSe Nanocrystal Quantum Dots: Intrinsic Limits to the Dark-Exciton Lifetime. *Appl. Phys. Lett.* **2003**, *82*, 2793–2795.
- (78) de Mello Donegá, C.; Bode, M.; Meijerink, A. Size- and Temperature-Dependence of Exciton Lifetimes in CdSe Quantum Dots. *Phys. Rev. B* **2006**, *74*, No. 085320.
- (79) Hoang, T. B.; Titova, L. V.; Jackson, H. E.; Smith, L. M.; Yarrison-Rice, J. M.; Lensch, J. L.; Lauhon, L. J. Temperature Dependent Photoluminescence of Single CdS Nanowires. *Appl. Phys. Lett.* **2006**, 89, 123123.
- (80) Furis, M.; Barrick, T.; Robbins, P.; Crooker, S. A.; Petruska, M.; Klimov, V.; Efros, A. L. Exciton Spin States in Nanocrystal Quantum Dots Revealed by Spin-Polarized Resonant Photoluminescence and Raman Spectroscopy. *Int. J. Mod. Phys. B* **2004**, *18*, 3769–3774.
- (81) Furis, M.; Htoon, H.; Petruska, M. A.; Klimov, V. I.; Barrick, T.; Crooker, S. A. Bright-Exciton Fine Structure and Anisotropic Exchange in CdSe Nanocrystal Quantum Dots. *Phys. Rev. B* **2006**, *73*, 241313.
- (82) De, C. K.; Routh, T.; Roy, D.; Mandal, S.; Mandal, P. K. Highly Photoluminescent InP Based Core Alloy Shell QDs from Air-Stable Precursors: Excitation Wavelength Dependent Photoluminescence Quantum Yield, Photoluminescence Decay Dynamics, and Single Particle Blinking Dynamics. *J. Phys. Chem. C* **2018**, *122*, 964–973.
- (83) Chung, H.; Choi, H.; Kim, D.; Jeong, S.; Kim, J. Size Dependence of Excitation-Energy-Related Surface Trapping Dynamics in PbS Quantum Dots. *J. Phys. Chem. C* **2015**, *119*, 7517–7524.
- (84) Li, B.; Brosseau, P. J.; Strandell, D. P.; Mack, T. G.; Kambhampati, P. Photophysical Action Spectra of Emission from Semiconductor Nanocrystals Reveal Violations to the Vavilov Rule Behavior from Hot Carrier Effects. *J. Phys. Chem. C* **2019**, 123, 5092–5098.
- (85) Martynenko, I. V.; Baimuratov, A. S.; Osipova, V. A.; Kuznetsova, V. A.; Purcell-Milton, F.; Rukhlenko, I. D.; Fedorov, A. V.; Gun'ko, Y. K.; Resch-Genger, U.; Baranov, A. V. Excitation Energy Dependence of the Photoluminescence Quantum Yield of Core/Shell CdSe/CdS Quantum Dots and Correlation with Circular Dichroism. *Chem. Mater.* **2018**, *30*, 465–471.

- (86) Mooney, J.; Krause, M. M.; Kambhampati, P. Connecting the Dots: The Kinetics and Thermodynamics of Hot, Cold, and Surface-Trapped Excitons in Semiconductor Nanocrystals. *J. Phys. Chem. C* **2014**, *118*, 7730–7739.
- (87) Righetto, M.; Minotto, A.; Bozio, R. Bridging Energetics and Dynamics of Exciton Trapping in Core—Shell Quantum Dots. *J. Phys. Chem. C* **2017**, *121*, 896–902.
- (88) Roy, D.; Das, A.; De, C. K.; Mandal, S.; Bangal, P. R.; Mandal, P. K. Why Does the Photoluminescence Efficiency Depend on Excitation Energy in Case of a Quantum Dot? A Case Study of CdSe-Based Core/Alloy Shell/Shell Quantum Dots Employing Ultrafast Pump—Probe Spectroscopy and Single Particle Spectroscopy. *J. Phys. Chem. C* 2019, 123, 6922—6933.
- (89) Hoheisel, W.; Colvin, V. L.; Johnson, C. S.; Alivisatos, A. P. Threshold for Quasicontinuum Absorption and Reduced Luminescence Efficiency in CdSe Nanocrystals. *J. Chem. Phys.* **1994**, *101*, 8455–8460.
- (90) Tonti, D.; van Mourik, F.; Chergui, M. On the Excitation Wavelength Dependence of the Luminescence Yield of Colloidal CdSe Quantum Dots. *Nano Lett.* **2004**, *4*, 2483–2487.
- (91) Zhang, Z.; Zhang, S.; Gushchina, I.; Guo, T.; Brennan, M. C.; Pavlovetc, I. M.; Grusenmeyer, T. A.; Kuno, M. Excitation Energy Dependence of Semiconductor Nanocrystal Emission Quantum Yields. J. Phys. Chem. Lett. 2021, 12, 4024—4031.
- (92) Geißler, D.; Würth, C.; Wolter, C.; Weller, H.; Resch-Genger, U. Excitation Wavelength Dependence of the Photoluminescence Quantum Yield and Decay Behavior of CdSe/CdS Quantum Dot/Quantum Rods with Different Aspect Ratios. *Phys. Chem. Chem. Phys.* **2017**, *19*, 12509–12516.